Published in final edited form as:
J Am Chem Soc. 2006 January 18; 128(2): 533–541. doi:10.1021/ja0549695.

Sulfur K-Edge XAS and DFT Calculations on Nitrile Hydratase: Geometric and Electronic Structure of the Non-heme Iron Active Site

Abhishek Dey[†], **Marina Chow**[†], **Kayoko Taniguchi**[§], **Priscilla Lugo-Mas**[⊥], **Steven Davin**[⊥], **Mizuo Maeda**[§], **Julie A. Kovacs**[⊥], **Masafumi Odaka**[§], **Keith O. Hodgson**[†,‡], **Britt Hedman**[‡], and **Edward I. Solomon**[†]

Edward I. Solomon: Edward.Solomon@stanford.edu

[†]Department of Chemistry, Stanford University, Stanford, California 94305

[§]Bioengineering Laboratory, RIKEN, Wako, Saitama 351-0198, Japan

[⊥]Department of Chemistry, University of Washington, Seattle, Washington 98195

[‡]Stanford Synchrotron Radiation Laboratory, SLAC, Stanford University, Stanford, California 94309

Abstract

The geometric and electronic structure of the active site of the non-heme iron enzyme nitrile hydratase (NHase) is studied using sulfur K-edge XAS and DFT calculations. Using thiolate (RS^-)-, sulfenate (RSO^-)-, and sulfinate (RSO_2^-)-ligated model complexes to provide benchmark spectral parameters, the results show that the S K-edge XAS is sensitive to the oxidation state of S-containing ligands and that the spectrum of the RSO^- species changes upon protonation as the S–O bond is elongated (by ~0.1 Å). These signature features are used to identify the three cysteine residues coordinated to the low-spin Fe^{III} in the active site of NHase as $CysS^-$, CysSOH, and $CysSO_2^-$ both in the NO-bound inactive form and in the photolyzed active form. These results are correlated to geometry-optimized DFT calculations. The pre-edge region of the X-ray absorption spectrum is sensitive to the Z_{eff} of the Fe and reveals that the Fe in $[FeNO]^6$ NHase species has a Z_{eff} very similar to that of its photolyzed Fe^{III} counterpart. DFT calculations reveal that this results from the strong π back-bonding into the π* antibonding orbital of NO, which shifts significant charge from the formally t_2^6 low-spin metal to the coordinated NO.

Introduction

Nitrile hydratase (NHase) hydrolyzes nitriles to amides and is used in the industrial preparation of acrylamide.[1–3] The active site can contain either a low-spin Fe^{III} or a low-spin Co^{III} ion coordinated by three cysteines and two deprotonated amides (two amides and two cysteines occupying the equatorial plane with an axial cysteine).[5–7] The Fe enzyme is

---

Correspondence to: Julie A. Kovacs; Masafumi Odaka; Keith O. Hodgson; Britt Hedman; Edward I. Solomon, `Edward.Solomon@stanford.edu`.

Supporting Information **Available:** Complete ref 47; optimized coordinates of complexes **1–4**, free ligands, and the NO active site of NHase (in gas phase and using the PCM model). This material is available free of charge via the Internet at http://pubs.acs.org.

isolated in a diamagnetic NO-bound form, activated by irradiation, and is proposed to be stabilized by the presence of butyric acid in the medium.[4] The sixth coordination site is occupied by a NO (as isolated) or an H_xO molecule (after photolysis).[8,9] In a recent crystal structure of the inactive NO-bound form[3a] (Figure 1a), the cysteine ligands are post-translationally modified to RSO-(H) and RSO_2(H) in contrast to a previously reported crystal structure showing non-oxidized $CysS^-$ coordination (Figure 1).[3b] However, aside from FT-IR, there are no direct spectroscopic probes of the $CysS^-$ ligand oxidation states in the active form of the enzyme.[10] Although active sites having transition-metal-bound oxidized thiolate residues are rare in nature, mutational studies on these thiolate residues have shown them to be catalytically relevant.[11,12]

The catalytic mechanism of this site is not well understood, and there are several proposals regarding the role of the low-spin Fe^{III} center in activating nitriles for hydrolysis.[13] The possible functional role of these modified cysteines, and the electronic structure of the as-isolated $[FeNO]^6$ species (using the Enemark–Feltham nomenclature, where the superscript 6 refers to the total number of valence electrons on the iron and the π* orbitals of NO) and its observed photochemistry, have been a focus of several recent experimental and theoretical studies.[14–18] A significant number of structurally relevant model complexes have been reported, some of which bind nitriles and some of which reversibly bind NO and show photolytic behavior.[19–22] Furthermore, the study of a series of model complexes having oxidized ligands has shown that this oxidation can significantly alter the pK_a of a water bound to the low-spin Fe^{III}.[23]

Ligand K-edge X-ray absorption spectroscopy (XAS) is a direct probe of a ligand's chemical nature and its bonding to a metal.[24,25] The primary transition at the K-edge is 1s → 4p. In the case of sulfur, transitions to other unoccupied antibonding orbitals, including the C–S σ*, O–S σ*, and M_{3d}–S antibonding orbitals, gain intensity due to sulfur 3p mixing. The observed intensity of these transitions is then directly proportional to the extent of this mixing.[26] This ligand K-edge XAS method has been used to investigate bonding in several models having different types of chlorine- and sulfur-based ligands and in the active sites of NiSOD and nickel dithiolenes, blue copper, Cu_A, and iron–sulfur proteins.[27–32] In those studies, where the focus was on the metal–sulfur bonding and its perturbation by the protein environment, it was found that the S K-edge is very sensitive to the Z_{eff} of a ligand, the chemical environment of the ligand, and the Z_{eff} of the metal to which it is bound.[33]

In this study we apply XAS and density functional theory (DFT) to a series of crystallographically characterized model complexes to identify signature spectroscopic features associated with thiolate-based ligands having different oxidation and protonation states. We then use these features to identify the ligands present in the active site of the protein NHase in its NO-bound inactive and photolyzed active forms. We further investigate the electronic structure of $[FeNO]^6$ NHase using DFT calculations in conjunction with the spectroscopic results.

Experimental Details

Sample Preparation

All four model complexes, $Fe^{III}(ADIT)_2$ (**1**), Fe^{III}(ADIT)(ADIT-O) (**2**), $[Co^{III}((\eta^2\text{-SO})(SO_2)N_3(Pr,Pr))]$ (**3**), and Fe^{III}-(ADIT)(ADIT-O-$ZnCl_3$) (**4**), were synthesized as reported in the literature.[19,34] For XAS experiments, the samples were ground into a fine powder, dispersed as thinly as possible on sulfur-free Mylar tape in a dry, anaerobic glovebox (N_2) atmosphere, and mounted across the window of an aluminum plate. This procedure has been verified to minimize self-absorption effects. A 6.35-µm polypropylene film window protected the solid samples from exposure to air during transfer from the glovebox to the experimental sample chamber.

The NO-bound NHase protein was expressed and purified as described in ref 35. The protein solutions (in 100 mM phosphate buffer, pH 7.5) were pre-equilibrated in a water-saturated He atmosphere for ~1 h to minimize bubble formation in the sample cell. The solution was loaded via a syringe into a Pt-plated Al block sample holder, sealed in front using a 6.3-µm polypropylene window. To ensure photolysis, the protein sample was illuminated by a 400-W tungsten lamp for 30 min before the XAS data measurements.

Data Collection and Reduction

XAS data were measured at the Stanford Synchrotron Radiation Laboratory using the 54-pole wiggler beam line 6-2. Details of the experimental configuration for low-energy studies have been described in an earlier publication.[33] The data reduction and error analysis follow the same method discussed previously.[36]

Fitting Procedure

Pre-edge features were fit by pseudo-Voigt line shapes (sums of Lorentzian and Gaussian functions). This line shape is appropriate as the experimental features are expected to be a convolution of a Lorentzian transition envelope and a Gaussian line shape imposed by the spectrometer optics.[37,38] A fixed 1:1 ratio of Lorentzian to Gaussian contribution successfully reproduced the pre-edge features. The rising edge was also fit with pseudo-Voigt line shapes. Good fits reproduce the data and its second derivative using a minimum number of peaks. The intensity of a pre-edge feature (peak area) is the sum of the intensity of all the pseudo-Voigt peaks which successfully fit the feature in a given fit. The reported intensity values for the proteins are averages of all good pre-edge fits.

Computational Details

All calculations were performed on dual-CPU Pentium Xeon 2.8 GHz work stations using the Amsterdam Density Functional (ADF) program, versions 2004.01, developed by Baerends et al.[39,40] A triple-ζ Slater-type orbital basis set (ADF basis set TZP) with a single polarization function at the local density approximation of Vosko, Wilk, and Nusair,[41] with nonlocal gradient corrections of Becke[42] and Perdew,[43] was employed. The molecular orbitals were plotted using Molden version 5.1, and the Mulliken[44] population analyses were performed using the AOMix[45] program. The calculations of the protein active site were performed using the BP86 functional as well as the hybrid B3LYP[46] functional with the

Gaussian 03 package.[47] The solvation calculations (single points and optimizations) were performed using the PCM[48] method and epsilon of 4.0. The optimizations were performed with a mixed basis set with 6-311g* on Fe, S, N, and O and 6-31g* on C and H. The single-point calculations were performed with a 6-311+g** basis set on all atoms.

Results and Analysis

A. S K-Edge XAS of Model Complexes and Free Ligands

The X-ray absorption spectra of the structurally characterized model complexes $[Fe^{III}(ADIT)_2]^+$ (**1**), $[Fe^{III}(ADIT)(ADIT\text{-}O)]^+$ (**2**), $[Co^{III}(\eta^2\text{-}SO)(SO_2)N_3(Pr,Pr)]^+$ (**3**), and $[Fe^{III}(ADIT)(ADITO\text{-}ZnCl_3)]^+$ (**4**) (Figure 2) were used as references for ligand oxidation state determination for the NHase enzyme (Figure 1).[49] Complex **1** contains a low-spin Fe^{III} atom coordinated by two thiolates, one of which is oxidized in the low-spin complex (**2**). Complex **4** has a $ZnCl_3$ moiety coordinated to the S–O moiety in **2**, while **3** has a low-spin Co^{III} atom ligated by an η^2-coordinated $S\text{–}O^-$ moiety and an RSO_2 moiety coordinated through sulfur, as in the proposed active site of NHase (Figure 1).[3]

The S K-edge XAS of free cysteine at pH 7.0 (black line in Figure 3) has an intense $RS^-{}_{1s} \rightarrow RS^-{}_{C\text{–}S\sigma*}$ transition at 2473.0 eV. The spectra of aqueous solutions of sulfinic acid at pH 12.0 (Figure 3, solid gray, deprotonated) and pH 1.3 (Figure 3, dashed gray, protonated) are almost identical, and the $RSO_2{}^-{}_{1s} \rightarrow RSO_2{}^-{}_{C\text{–}S\sigma*}$ and $RSO_2{}^-{}_{1s} \rightarrow RSO_2{}^-{}_{O\text{–}S\sigma*}$ transitions show up as a strong absorption feature at 2477.0 eV. The shift of this feature from 2473 eV in cysteine to 2477 eV in sulfinic acid reflects the stabilization of the S_{1s} orbital due to the higher oxidation state of sulfur in the latter.[33,50] The S K-edge XAS of complex **1** (Figure 3, solid blue) shows two pre-edge transitions around 2470 eV (2469.8 and 2470.5 eV) and a transition at 2473.1 eV, corresponding to $RS^-{}_{1s} \rightarrow Fe_{3d}$ and $RS^-{}_{1s} \rightarrow RS^-{}_{C\text{–}S\sigma*}$ transitions, respectively. The spectrum of complex **2** (Figure 3, dashed blue) also shows the two pre-edge transitions from the thiolate (now well separated) at 2469.8 and 2470.9 eV and an $RS^-{}_{1s} \rightarrow RS^-{}_{C\text{–}S\sigma*}$ transition at 2473.3 eV, as well as a new third broad transition with a maximum at 2475.3 eV, which is now assigned to an envelope of the $RSO^-{}_{1s} \rightarrow RSO^-{}_{C\text{–}S\sigma*}$ and $RSO^-{}_{1s} \rightarrow RSO^-{}_{O\text{–}S\sigma*}$ transitions. These transitions are shifted higher in energy relative to the $RS^-{}_{1s} \rightarrow RS^-{}_{C\text{–}S\sigma*}$ transitions due to the deeper energy of the 1s orbital of the oxidized sulfur in RSO^-. Note that the $RSO^-{}_{1s} \rightarrow Fe_{3d}$ pre-edge transition should also have intensity due to covalent bonding of the RSO^- ligand to the metal d-orbitals through the sulfur. However, this would largely overlap the $RS^-{}_{1s} \rightarrow RS^-{}_{C\text{–}S\sigma*}$ transition at 2473.1 eV in **2**. This transition is, in fact, clearly observed at 2473.2 eV for **3** (Figure 3, red), a complex in which there is no RS^- ligand and hence no $RS^-{}_{1s} \rightarrow RS^-{}_{C\text{–}S\sigma*}$ transition. As for **2**, complex **3** also exhibits $RSO^-{}_{1s} \rightarrow RSO^-{}_{C\text{–}S\sigma*}$ and $RSO^-{}_{1s} \rightarrow RSO^-{}_{O\text{–}S\sigma*}$ transitions at ~2475 eV (maxima at 2474.9 and 2475.9 eV). There is an additional higher-energy feature in the spectrum of **3** at 2478.8 eV, which is assigned to the $RSO_2{}^-{}_{1s} \rightarrow RSO_2{}^-{}_{C\text{–}S\sigma*}$ and $RSO_2{}^-{}_{1s} \rightarrow RSO_2{}^-{}_{O\text{–}S\sigma*}$ transitions. Note that this transition envelope is shifted up in energy by almost 2 eV for complex **3** (2478.8 eV, Figure 3, red) relative to free sulfinic acid (2477.0 eV, Figure 3, solid gray). This shift has contributions from both the increase in Z_{eff} of sulfur in $RSO_2{}^-$ due to its covalent bonding to the Co^{III} ion, which shifts the sulfur 1s orbital to deeper energy, and from the shorter S–O bonds in **3** (1.45 Å) compared to the those in the free ligand (1.51 Å), which shifts the σ* orbital to higher energy (Table 1). The XAS of complex **4** (Figure 3, green) is very similar to that of **2** (Figure 3, dashed blue) and has the same assignment of features, i.e., $RS^-_{1s} \rightarrow Fe_{3d}$ and $RS^-_{1s} \rightarrow RS^-_{C–S\sigma*}$ transitions around 2470 and 2473 eV, respectively, and $RSO^-_{1s} \rightarrow RSO^-_{C–S\sigma*}$ and $RSO^-_{1s} \rightarrow RSO^-_{O–S\sigma*}$ transitions at 2474.9 and 2475.9 eV, respectively.

It is also important to note that the broad, higher-energy transition at ~2475 eV in **2**, associated with the $RSO^-_{1s} \rightarrow RSO^-_{C–S\sigma*}$ and $RSO^-_{1s} \rightarrow RSO^-_{O–S\sigma*}$, is partly split in **3** and is clearly split into two features, at 2474.9 and 2475.9 eV, in **4**. Note that complexes **3** and **4** both have the oxygen atom of the RSO^- coordinated to a metal (Co^{III} in **3** and Zn^{II} in **4**), and this interaction appears to energy-split the broad feature at ~2475 eV. DFT calculations were used to evaluate the effects of metal coordination to the S, protonation/metal coordination to the O of RSO^-, and protonation of RSO_2^-.

B. DFT Calculations of the Model Complexes and Ligands

Geometry-optimized DFT calculations were performed for complexes **2** and **3** and for the free ligands CH_3SO^-, CH_3SOH, $CH_3SO_2^-$, and CH_3SO_2H. The optimized bond lengths are in overall good agreement with published crystal structures (Table 1). The optimized structures are used to obtain ground-state S_{3p} orbital distributions in the unoccupied virtual orbitals for these complexes and free ligands. These calculations were used to estimate the relative energies (zero defined as 2390 eV) and intensities of their S K-edge XAS (Figure 4, predicted S K-edge).[51] Though the absolute transition energies were under-estimated (due to lack of relativistic corrections), the relative energies of the pre-edge and the rising edge features are in good agreement with the experimental spectra in Figure 3.

The intensity distribution for **2** (Figure 4, dashed blue) shows two features corresponding to $RS^-_{1s} \rightarrow Fe_{3d}$ and $RS^-_{1s} \rightarrow RS^-_{C–S\sigma*}$ transitions at 4.0 eV (first transition split due to ligand field effects on the 3d orbitals) and 7.0 eV, respectively. It also shows a third feature at 9.0 eV which corresponds to contributions of the $RSO^-_{1s} \rightarrow RSO^-_{C–S\sigma*}$ and $RSO^-_{1s} \rightarrow RSO^-_{O–S\sigma*}$ transitions. Calculations for complex **3** give the $RSO^-_{1s} \rightarrow Co_{3d}$ transition at 6.3 eV and the $RSO^-_{1s} \rightarrow RSO^-_{C–S\sigma*}$ and $RSO^-_{1s} \rightarrow RSO^-_{O–S\sigma*}$ transitions at 9.0 eV (Figure 4, red). Note that the σ* transitions are separated in energy by 1 eV and that the calculations reproduce the experimentally observed energy splitting of this feature. There is an additional higher-energy feature for **3** (Figure 4, red), corresponding to the overlapping contributions from $RSO_2{}^-{}_{1s} \rightarrow RSO_2{}^-{}_{C–S\sigma*}$ and $RSO_2{}^-{}_{1s} \rightarrow RSO_2{}^-{}_{O–S\sigma*}$ transitions. Calculations on both free $CH_3SO_2^-$ and CH_3SO_2H show this feature at 9–11 eV (Figure 4, solid gray and dashed gray, respectively). These calculations reproduce the 2-eV increase in energy of this feature observed in the data for **3** relative to that of the free ligand and show no significant effect of protonation of the oxygen of the RSO_2^- group on the S_{3p} distribution, consistent with experiment (Figure 3, solid gray and dashed gray). A calculation performed on the $CH_3SO_2^-$ fragment, having the geometry of complex **3** (i.e., with shorter S–O bond lengths) but not coordinated to a metal ion, shows no significant shift of the $RSO_2{}^-{}_{1s} \rightarrow RSO_2{}^-{}_{C–S\sigma*}$ and $RSO_2{}^-{}_{1s} \rightarrow RSO_2{}^-{}_{O–S\sigma*}$ transition energies, indicating that the experimentally observed 2-eV shift of this feature between the free ligand and complex **3** (Figure 3, red and gray lines) is a result of Co^{III} coordination to the sulfur of RSO_2^-. This shifts charge density from S to Co^{III}, stabilizing the S 1s orbital energy in complex **3** relative to that of the free ligand.

A DFT calculation on CH_3SO^- shows one feature at 7.0 eV that corresponds to an envelope of the $RSO^-_{1s} \rightarrow RSO^-_{C–S\sigma*}$ and $RSO^-_{1s} \rightarrow RSO^-_{O–S\sigma*}$ transitions (Figure 4, green).[52] In contrast to calculations on $RSO_2(H)$, the DFT calculation on the free CH_3SOH ligand shows dramatic differences in the S_{3p} energy/intensity distribution relative to that of the CH_3SO^- ligand. The $RSO^-_{1s} \rightarrow RSO^-_{C–S\sigma*}$ and $RSO^-_{1s} \rightarrow RSO^-_{O–S\sigma*}$ transitions, which combine into one peak at 7.0 eV in the deprotonated ligand (Figure 4, solid green), are now split into two peaks (Figure 4, dashed green) at 6.0 eV (the $RSO^-_{1s} \rightarrow RSO^-_{O–S\sigma*}$ transition) and 8.0 eV (the $RSO^-_{1s} \rightarrow RSO^-_{C–S\sigma*}$ transition) upon protonation. Geometry-optimized DFT calculations on these free ligands (Table 1) show that the C–S bond shortens by 0.06 Å and the S–O bond elongates by 0.1 Å on protonation of CH_3SO^-. This shifts the C–S σ* orbital higher and the O–S σ* orbital lower in energy, resulting in the observed energy splitting of these features. A similar elongation of the S–O and shortening of the C–S bonds is observed in complexes **4** and **3** (O–S 1.56 Å, C–S 1.86 Å and O–S 1.57 Å, C–S 1.87 Å, respectively) relative to **2** (O–S 1.55 Å, C–S 1.85 Å).[53] Thus, the experimentally observed energy splitting of the 2474–2476 eV features of complexes **3** and **4** is due to the weakening of the S–O and strengthening of the C–S bonds as a result of the metal coordination to the RSO^- oxygen atom. The larger energy splitting for complex **4** is probably due to its stronger coordination to Zn^{II}. As shown in Figure 4, full protonation produces the largest effect. It should be noted that for $RSO_2(H)$ the changes in bond lengths with protonation are smaller (1.53 Å vs 1.49 and 1.69 Å) and the split of the feature at 9–11 eV does not change significantly.

In summary, from the model studies it is found that the S1s → C–S σ* and S–O σ* transitions are very sensitive to the Z_{eff} of the sulfur. RS^- has $RS^-_{1s} \rightarrow Fe_{3d}$ and $RS^-_{1s} \rightarrow RS^-_{C–S\sigma*}$ transitions at ~2470 and ~2473 eV, respectively, RSO^- has $RSO^-_{1s} \rightarrow RSO^-_{C–S\sigma*}$ and $RSO^-_{1s} \rightarrow RSO^-_{O–S\sigma*}$ transitions at 2475 eV which split by 2 eV on protonation, and RSO_2^- has the $RSO_2^-{}_{1s} \rightarrow RSO_2^-{}_{C–S\sigma*}$ and $RSO_2^-{}_{1s} \rightarrow RSO_2^-{}_{O–S\sigma*}$ transitions at 2477–2479 eV (depending on metal ion coordination) which are not significantly affected by protonation.

C. S K-Edge XAS of Nitrile Hydratase

The S K-edge XAS of the inactive NO-bound form of NHase shows four distinct features (Figure 5, black). The lowest-energy feature, at 2470.1 eV (inset), is assigned as the $RS^-_{1s} \rightarrow Fe_{3d}$ transition. The broad envelope at 2472–2474 eV can be assigned as a composite of $RS^-_{1s} \rightarrow RS^-_{C–S\sigma*}$ transitions of the ligated cysteine, two free cysteines and nine methionines. The other higher-energy features, at 2476.1 and 2478.5 eV, are relatively weak; however, a simulated spectrum generated by the normalized addition of the spectra of aqueous methionine and cysteine at pH 7.5 and **1**, representing thiolate coordination but no oxidized sulfur (Figure 5, blue), shows no higher-energy features. Alternatively, simulation including the oxidized ligands (Figure 5, red, complex **3**) shows two higher-energy features at 2475–2476 and 2475.5–2479.5 eV, similar to those for NHase-NO at 2476.1 and 2478.5 eV, indicating that they are associated with the oxidized sulfur ligands present in the NO-bound form of the protein. The feature at 2478.5 eV for the enzyme can be assigned to RSO_2^-. Note that this is at a higher energy than for the $RSO_2{}^-{}_{1s} \rightarrow RSO_2{}^-{}_{C\text{–}S\sigma*}$ and $RSO_2{}^-{}_{1s} \rightarrow RSO_2{}^-{}_{O\text{–}S\sigma*}$ transitions observed for the free RSO_2^- ligand (at 2476–2478 eV, Figure 3, gray) but lower than those for the Co^{III} complex **3** (at 2478.8 eV, Figure 3, red), indicating coordination of the $CysSO_2^-$ ligand at the protein active site but with a weaker bond relative to complex **3**.

The feature at 2476.1 eV could originate from RSO^-, although this feature is shifted to higher energy by ~1 eV than is observed for RSO^- in complexes **2** and **3**. In sections A and B (vide supra), it is shown that the energy of the RSO^- feature is sensitive to the chemical environment of the oxygen. Inspection of the second derivatives of the absorption data (where minima in second derivative represent maxima in the absorption spectrum) (Figure 6) reveals that the NHase-NO enzyme data has a minimum at 2476.1 eV (Figure 6, black), while the RSO^--ligated complex (**2**) has a broad minimum at 2475.2 eV (Figure 6, dashed blue). In **4** (Figure 6, green), where Zn^{2+} is strongly bound to the O of RSO^-, the $RSO^-{}_{1s} \rightarrow RSO^-{}_{S\text{–}O\sigma*}$ feature has shifted down to 2474.8 eV, reflecting a weaker S–O bond in **4**, while the $RSO^-{}_{1s} \rightarrow RSO^-{}_{C\text{–}S\sigma*}$ negative feature remains at 2476.1 eV. As found in section B, protonation of RSO^- will shift the S–O σ* transition to 2 eV lower in energy than the C–S σ* transition, due to the elongation of the S–O bond. Hence, the absence of a single minimum in the second derivative, corresponding to a peak in absorption between 2474 and 2475 eV in the NHase data, argues against the presence of an RSO^- residue and indicates that the cysteine sulfenic acid residue in the NHase active site is protonated. While the $RSO(H)_{1s} \rightarrow RSO(H)_{C\text{–}S\sigma*}$ transition is observed in the data for NHase (Figure 6, black) at 2476.1 eV, about 1.0 eV higher than the single peak observed for **2** (which can be used as an estimate of the energy position of a pure RSO^- feature), the $RSO(H)_{1s} \rightarrow RSO(H)_{S\text{–}O\sigma*}$ transition of Nhase, which is estimated to be 2 eV lower in energy relative to the $RSO(H)_{1s} \rightarrow RSO(H)_{C\text{–}S\sigma*}$ transition, could be merged into the $RS^-{}_{1s} \rightarrow RS^-{}_{C\text{–}S\sigma*}$ transition envelope at 2472–2474 eV.[54]

S K-edge XAS data for the photoactivated protein (Figure 5, dashed black) show no significant change relative to the data for the inactive NO-bound NHase. This indicates that the oxidation states of the metal and the sulfur ligands and the protonation state of RSO^- are virtually identical in the NO-bound inactive and the photolyzed active enzyme. However, there is a markedly increased pre-edge intensity upon photolysis (Figure 5, inset), which is analyzed in section E.

D. DFT Calculations on the Active Site of NHase

While the S K-edge XAS data for the protein active site and model complexes enabled us to assign the chemical nature of two of the three cysteinyl ligands ($CysS^-$ and CysSOH), it could not help to discern the protonation state of the $CysSO_2^-$ ligand. Geometry-optimized DFT calculations were performed on the crystallographically characterized NO-bound inactive form to evaluate this issue (Figure 7A). The active site was modeled using two oxidized cysteines coordinated to the Fe in the equatorial plane (Cys 114, Cys 112) and a methyl thiolate modeling the axial cysteine (Cys 109). There are two hydrogen bonds from nearby arginine residues (Arg 141 and Arg 56) which are modeled by two $C(NH_2)_3^+$

fragments.[55] The optimized structures show that the $CysSO_2^-$ remains in its ionized form. This is reasonable as the pK_a of RSO_2^- is 6–7 and that of arginine is 12–14; hence, they are expected to be ionized under the experimental conditions. Also, in a vacuum the charged species should neutralize while they may not do so in a PCM calculation. On the contrary, the proton from the $C(NH_2)_3^+$ fragment, H-bonding to $CysSO^-$, shifts to the $CysSO^-$ oxygen, producing a neutral CysSOH species (Figure 7B). This computational model agrees well with the geometric structure obtained from the XAS data as the optimized geometry displays a long (1.68 Å) S–O bond upon protonation, which will split the $RSO^-_{1s} \rightarrow RSO^-_{C\text{–}S\sigma*}$ and $RSO^-_{1s} \rightarrow RSO^-_{O\text{–}S\sigma*}$, as observed experimentally. However, it must be noted that the pK_a of the RSO^- residue is 10–11 and that for arginine is 12–14.[56] As indicated above, the protonation state of the arginine-CysSO unit will depend on the dielectric constant of the medium. Geometry optimizations were also performed using a PCM solvation model with an epsilon of 4.0. The results of this optimization show that the $CysSO^-$ and the $C(NH_2)_3^+$ residues remain charge-separated after optimization (Figure 7C), in contrast to the vacuum-based calculations and the experimental results from XAS. However, the energy difference between the CysSOH–$C(NH_2)_2$(NH) and the $CysSO^-$–$C(NH_2)_3^+$ forms is only 4 kcal/mol and depends on modeling of the active site and the functional used (4 kcal/mol for B3LYP and 7 kcal/mol for BP86).[57] This energy difference corresponds to a pK_a difference of 3 units. An electrostatic calculation (not included in the DFT modeling) of the pK_a's for the buried arginines in Nhase shows that these vary over the range 16.6 (the surface residues have ~12) to 8.5, with one of the two (Arg 167) H-bonded to the SO^- ligand having a pK_a of 9.3.[58]

E. Pre-edge Analysis

Due to covalent interaction with the axial $CysS^-$, the unoccupied 3d orbitals of the NO-bound NHase active site will have S_{3p} mixing, and hence will exhibit $RS^-_{1s} \rightarrow Fe_{3d}$ transition intensity, which is proportional to the coefficient of S_{3p} mixing in these orbitals. The S K-edge XAS of the NO-bound inactive form has a distinct pre-edge feature with a maximum at 2470.0 eV (Figure 6, inset, black). The renormalized intensity of this pre-edge feature is 0.69 unit, which correspond to 20% S_{3p} character mixed into the antibonding 3d orbital (Table 2). The NHase-photoactivated sample has two pre-edge features, one at 2469.6 eV and a second at 2470.2 eV, with 0.31 and 0.51 unit of intensity, respectively (Figure 6, inset, dashed black). This indicates that the active site of the photolyzed form has two 3d antibonding orbitals with 9% and 15% S_{3p} character (Table 2).

The MO diagrams of the NO-bound ($[FeNO]^6$) and photolyzed NHase are given in Figure 8 (the β unoccupied orbitals). Figure 8 (right) shows that the NO-bound form has a formal t_2^6 configuration. There are two unoccupied NO π* LUMOs and two higher-energy unoccupied e orbitals, d_{z^2} and $d_{x^2-y^2}$. The d_{z^2} orbital (highlighted in blue) has 19% S_{3p} character due to *pseudo*-σ (S_{3p} orbital slightly tilted off the Fe–S bond as the angle C–S–Fe > 90°) overlap with the thiolate, which would provide the intensity for a single pre-edge feature, as observed in Figure 6 (inset) at 2470.1 eV. Photolysis cleaves the Fe–NO bond and creates a low-spin Fe^{III} center with a H_2O/OH^- molecule coordinated in place of NO. Here the t_2 hole is oriented by the strong axial $CysS^-$ donor into the d-π orbitals (shaded in red). This covalent mixing of the $CysS^-$ π into the d orbital leads to the new lower-energy feature at

2469.5 eV in the pre-edge of the photolyzed protein. The higher-energy e feature remains at 2470.2 eV, as the pseudo-σ overlap with this axial $CysS^-$ ligand does not change.

The pre-edge region of the S K-edge XAS data is affected by the chemical nature of the ligand, the ligand field of the metal, and its Z_{eff}. Here we use the pre-edge to probe the Z_{eff} of the metal ion and thus obtain insight into its effective oxidation state. It is important to note that Fe^{II} complexes do not show a pre-edge transition, as the Z_{eff} for the Fe^{II} is low and this shifts the Fe_{3d} manifold of orbitals to higher energy, such that the $RS^-_{1s} \rightarrow Fe_{3d}$ transitions overlap with the $RS^-_{1s} \rightarrow RS^-_{C–S\sigma*}$ transition and are not distinguishable. The fit to the NHase data shows a small pre-edge feature at 2470.1 eV (Figure 5 inset, Table 2), which suggests that the Z_{eff} of the Fe in the $[FeNO]^6$ active site of NHase is significantly higher than that for low-spin Fe^{II} complexes[59] and similar to that of Fe^{III} NHase.

Discussion

S K-edge XAS is very sensitive to the chemical nature of the sulfur atom. In this study we have used structurally characterized synthetic model complexes to identify signature transitions corresponding to different types of sulfur ligands. Not only does the edge show dramatic differences upon oxidation; in the case of RSO^- the edge is also sensitive to protonation. The data for both the NO-bound inactive and photolyzed active forms of the NHase enzyme show the presence of three types of sulfur ligands at the active site: $CysS^-$, CysSOH, and $CysSO_2(H)$. Although we could not identify the protonation state of the $CysSO_2^-$ using our data, DFT calculations in both the gas phase and PCM show that it is ionized (Figure 9). This model can now be used to understand the role of these oxidized cysteines in catalysis.

The oxidation of the cysteine ligands has been proposed to be catalytically relevant, either by affecting the binding of a nitrile, followed by a nucleophilic attack by H_2O, or by affecting the binding of a H_2O to the open coordination site of the Fe, which then ionizes to release a H^+ that catalyzes the hydrolysis. A geometry-optimized DFT calculation on a low-spin Fe^{III} NHase active site with three thiolates (Figure 10) and using H_2O as the sixth ligand shows weak binding ($Fe–OH_2 = 3.4$ Å) affinity. However, calculations with the oxidized ligand set show favorable H_2O binding in this vacant coordination site ($Fe–OH_2 = 2.1$ Å). Thus, the oxidized sulfur ligands are weaker donors, which will increase the Lewis acidity of the Fe^{III} center and thus tune the ligand binding affinity to this vacant, catalytically relevant, exchangeable coordination site.

The electronic structure of linear $[FeNO]^6$ units has been a major focus of research in bio-inorganic chemistry.[60,61] Münck and co-workers, using Mössbauer spectroscopy, suggested that the electronic structure of the NO-bound NHase can be described as $Fe(IV)\text{-}NO^-$.[62] That conclusion was based on small isomer shifts (0.03–0.05 mm/s) and high quadrupole splittings (1.3–2.0 mm/s) observed for an $[FeNO]^6$ model.[63] However, the electronic properties of these complexes, investigated by recent DFT calculations, have suggested that this unit can be described as a low-spin Fe^{2+} coordinated to a NO^+ unit.[60,64] On photolysis, a low-spin Fe^{III} center is produced which is well-characterized by EPR, Mössbauer, and resonance Raman spectroscopy.[1,6] Note that, from the XAS near-edge transitions, we know that the chemical nature of the $CysS^-$ does not change upon photolysis, and hence it serves as a spectator of the change in Z_{eff} of the Fe ion in this process. The pre-edge of this photolyzed ferric active site is observed at 2469–2470 eV (Figure 6, inset, dashed black), an energy very similar to that of the pre-edge of the inactive NO-bound form of NHase. This suggests that the Z_{eff} of the Fe atom in the $[FeNO]^6$ NHase active site is very similar to that of Fe^{III} NHase rather than to that of Fe^{II} or Fe^{IV}. Also note that the second derivative of the NO-bound form (Figure 6 inset, black) has only one feature at 2470.1 eV, corresponding to one $RS^-{}_{1s} \rightarrow Fe_{3d}$ (e) transition, while the second derivative of the photolyzed protein has an additional feature in the pre-edge at 2469.5 eV, corresponding to the creation of a new low-energy t_2 hole in forming the low-spin Fe^{III} center. This suggests that the $[FeNO]^6$ unit of inactive NHase has a Z_{eff} similar to that of Fe^{III} but does not have a t_2 hole. Such an electronic structure would be consistent with strong back-donation from the low-spin t_2^6 iron to NO π^* orbitals. From Figure 8, the inactive NO-bound form has a low-spin t_2^6 iron center that has 28–31% back-bonding interaction with the NO (3d character summed over two unoccupied NO π^* orbitals), which shifts charge density from the formally Fe^{II} and increases its Z_{eff}.

Supplementary Material

Refer to Web version on PubMed Central for supplementary material.

Acknowledgment

This research was supported by NIH Grants NIH GM-40392 (E.I.S.), RR-01209 (K.O.H.), and GM45881 (J.A.K.) and by the Bioarchitect Research Program, RIKEN (M.O.). P.L.-M. gratefully acknowledges support from NIH Predoctoral Minority Fellowship F31-GM073583-01. SSRL operations are supported by the Department of Energy, Office of Basic Energy Sciences. The SSRL Structural Molecular Biology Program is supported by the National Institutes of Health, National Center for Research Resources, Biomedical Technology Program, and by the Department of Energy, Office of Biological and Environmental Research.

References

1. Endo I, Nojiri M, Tsujimura M, Nakasako M, Nagashima S, Yohda M, Odaka M. J. Inorg. Biochem. 2001; 83:247–253. [PubMed: 11293544]
2. Yamada H, Kobayashi M. Biosci. Biotechnol. Biochem. 1996; 60:1391–1400. [PubMed: 8987584]
3. (a) Nagashima S, Nakasako M, Dohmae N, Tsujimura M, Takio K, Odaka M, Yohda M, Kamiya N, Endo I. Nat. Struct. Biol. 1998; 5:347–351. [PubMed: 9586994] (b) Huang W, Jia J, Cummings J, Nelson M, Schneider G, Lindqvist Y. Structure. 1997; 5:691–699. [PubMed: 9195885]
4. Nagasawa T, Takeuchi K, Yamada H. Eur. J. Biochem. 1991; 196:581–589. [PubMed: 2013281]
5. Payne MS, Wu S, Fallon RD, Tudor G, Stieglitz B, Turner IM, Nelson MJ. Biochemistry. 1997; 36:5447–5454. [PubMed: 9154927]
6. Miyanaga A, Fushinobu S, Ito K, Shoun H. Eur. J. Biochem. 2004; 271:429–438. [PubMed: 14717710]
7. Watanabe N, Nakayama H, Odaka M, Kawano Y, Takio K, Kamiya N, Nagamune T, Endo I. J. Inorg. Biochem. 2001; 86:475–475.
8. Odaka M, Fujii K, Hoshino M, Noguchi T, Tsujimura M, Nagashima S, Yohda M, Nagamune T, Inoue Y, Endo I. J. Am. Chem. Soc. 1997; 119:3785–3791.
9. Endo I, Odaka M, Yohda M. Trends Biotechnol. 1999; 17:244–248. [PubMed: 10354562]
10. Noguchi T, Nojiri M, Takei K, Odaka M, Kamiya N. Biochemistry. 2003; 42:11642–11650. [PubMed: 14529274]

11. Murakami T, Nojiri M, Nakayama H, Odaka M, Yohda M, Dohmae N, Takio K, Nagamune T, Endo I. Protein Sci. 2000; 9:1024–1030. [PubMed: 10850812]
12. Piersma SR, Nojiri M, Tsujimura M, Noguchi T, Odaka M, Yohda M, Inoue Y, Endo I. J. Inorg. Biochem. 2000; 80:283–288. [PubMed: 11001100]
13. Endo I, Nojiri M, Tsujimura M, Nakasako M, Nagashima S, Yohda M, Odaka M. J. Inorg. Biochem. 2001; 83:247–253. [PubMed: 11293544]
14. Mascharak PK. Coord. Chem. ReV. 2002; 225:201–214.
15. Kobayashi M, Shimizu S. Eur. J. Biochem. 1999; 261:1–9. [PubMed: 10103026]
16. Boone AJ, Chang CH, Greene SN, Herz T, Richards NGJ. Coord. Chem. ReV. 2003; 238:291–314.
17. Harrop TC, Mascharak PK. Acc. Chem. Res. 2004; 37:253–260. [PubMed: 15096062]
18. Grapperhaus CA, Patra AK, Mashuta MS. Inorg. Chem. 2002; 41:1039–1041. [PubMed: 11874334]
19. Kovacs JA. Chem. ReV. 2004; 104:825–848. [PubMed: 14871143]
20. Shearer J, Kung IY, Lovell S, Kaminsky W, Kovacs JA. J. Am. Chem. Soc. 2001; 123:463–468. [PubMed: 11456548]
21. Shearer J, Jackson HL, Schweitzer D, Rittenberg DK, Leavy TM, Kaminsky W, Scarrow RC, Kovacs JA. J. Am. Chem. Soc. 2002; 124:11417–11428. [PubMed: 12236756]
22. Noveron JC, Olmstead MM, Mascharak PK. J. Am. Chem. Soc. 2001; 123:3247–3259. [PubMed: 11457060]
23. Tyler LA, Noveron JC, Olmstead MM, Mascharak PK. Inorg. Chem. 2003; 42:5751–5761. [PubMed: 12950226]
24. Solomon EI, Hedman B, Hodgson KO, Dey A, Szilagyi RK. Coord. Chem. ReV. 2005; 249:97–129.
25. Glaser T, Hedman B, Hodgson KO, Solomon EI. Acc. Chem. Res. 2000; 33:859–868. [PubMed: 11123885]
26. Neese F, Hedman B, Hodgson KO, Solomon EI. Inorg. Chem. 1999; 38:4854–4860. [PubMed: 11671216]
27. Szilagyi RK, Bryngelson PA, Maroney MJ, Hedman B, Hodgson KO, Solomon EI. J. Am. Chem. Soc. 2004; 126:3018–3019. [PubMed: 15012109]
28. George SD, Metz M, Szilagyi RK, Wang HX, Cramer SP, Lu Y, Tolman WB, Hedman B, Hodgson KO, Solomon EI. J. Am. Chem. Soc. 2001; 123:5757–5767. [PubMed: 11403610]
29. Szilagyi RK, Lim BS, Glaser T, Holm RH, Hedman B, Hodgson KO, Solomon EI. J. Am. Chem. Soc. 2003; 125:9158–9169. [PubMed: 15369373]
30. Anxolabéhère-Mallart E, Glaser T, Frank P, Aliverti A, Zanetti G, Hedman B, Hodgson KO, Solomon EI. J. Am. Chem. Soc. 2001; 123:5444–5452. [PubMed: 11389625]
31. Dey A, Glaser T, Moura JJG, Holm RH, Hedman B, Hodgson KO, Solomon EI. J. Am. Chem. Soc. 2004; 126:16868–16878. [PubMed: 15612726]
32. Glaser T, Bertini I, Moura JJG, Hedman B, Hodgson KO, Solomon EI. J. Am. Chem. Soc. 2001; 123:4859–4860. [PubMed: 11457306]
33. Hedman B, Frank P, Gheller SF, Roe AL, Newton WE, Hodgson KO. J. Am. Chem. Soc. 1988; 110:3798–3805.
34. Lugo-Mas P, Xu L, Davin SD, Benedict J, Kaminsky W, Kovacs JA. J. Am. Chem. Soc. submitted.
35. Nojiri M, Yohda M, Odaka M, Matsushita Y, Tsujimura M, Yoshida T, Dohmae N, Takio K, Endo I. J. Biochem. 1999; 125:696–704. [PubMed: 10101282]
36. Shadle SE, Hedman B, Hodgson KO, Solomon EI. Inorg. Chem. 1994; 33:4235–4244.
37. Agarwal, BK. X-ray Spectroscopy. Berlin: Springer-Verlag; 1979. p. 276 ff
38. Tyson TA, Roe AL, Frank P, Hodgson KO, Hedman B. Phys. ReV. B. 1989; 39A:6305–6315.
39. Baerends EJ, Ellis DE, Roos P. Chem. Phys. 1973; 2:41–51.
40. te Velde G, Baerends EJ. Int. J. Comput. Phys. 1992; 99:84–98.
41. Vosko SH, Wilk L, Nusair M. Can. J. Phys. 1980; 58:1200–1211.

42. Becke AD. Phys. ReV. A: Gen. Phys. 1988; 38:3098–3100.

43. Perdew JP. Phys. ReV. B. 1986; 33:8822–8224.

44. Mulliken RS. J. Chem. Phys. 1955; 23:1833–1840.

45. Gorelsky SI. AOMix Program rev.6.04. (http://www.sg-chem.net). Gorelsky SI, Lever ABP. J. Organomet. Chem. 2001; 635:187–196.

46. Becke AD. J. Chem. Phys. 1993; 98:5648–5652.

47. Frisch, MJ., et al. Gaussian 03, Revision C.02. Wallingford CT: Gaussian, Inc.; 2004.

48. Miertus S, Scrocco E, Tomasi J. Chem. Phys. 1981; 55:117–129.

49. The S K-edge XAS of free ligands having varying oxidation states is given in Figure S1 in the Supporting Information for reference. These results were published in ref 33.

50. XAS data for a stable uncoordinated RSO^- species were unavailable, so we used the model complex data to identify the spectroscopic feature of this ligand.

51. The calculated S_{3p} characters were scaled up by an approximate factor of 2 for every two units of change in its oxidation number to account for the increase in Z_{eff}, which will increase the transition dipole integral, i.e. $\langle S_{1s}|\mathbf{r}|S_{3p}\rangle$, leading to an increase in absorption intensity.

52. This transition is not shifted in energy in the CH_3SO^- fragment having the geometric parameters of complex **2**, but *is* shifted (by 1.6 eV) to 8.9 eV in **2**, reflecting the shift of charge from the coordinated sulfur atom due to covalent interaction, as also observed in complex **3**.

53. The optimized S–O bond in **2** is 0.04 Å longer than in the crystal structure, while those for **3** and **4** are within 0.01 Å (Table 1).

54. Note that there is a minimum in the protein XAS data at 2474 eV, which may originate from $RSO^-{}_{1s} \rightarrow RSO^-{}_{S\text{–}O\sigma^*}$. However, in the presence of nine methionine residues this feature is not observed in the absorption data.

55. The central C of the $C(NH_2)_3{}^+$ species was frozen during optimization.

56. Okuyama T, Miyake K, Fueno T, Yoshimura T, Soga S, Tsukurimichi E. Heteroat. Chem. 1992; 3:577–583.

57. Given the resolution of the crystal structure, it is not possible to distinguish between calculated structures B ($\varepsilon = 0$) and C ($\varepsilon = 4.0$) using structural parameters.

58. Estimated using the crystal structure of NO bound Nhase (pdb id 2AHJ) with the software PROPKA: Li H, Robertson AD, Jensen Jan H. Proteins. 2005; 61:704–721. [PubMed: 16231289]

59. The absence of a pre-edge feature in Fe^{II} sites has been studied in complexes with weak field ligands (Cl^- RS^-). Here, the 3d manifold in the NHase-NO complex will be further shifted to higher energy by the strong amide and NO donors. Hence, the pre-edge transition will shift deeper into the $RS_{1s} \rightarrow RS_{C\text{–}S\sigma^*}$ transitions of the rising edge. Thus, the spin state cannot account for the low pre-edge energy.

60. Serres RG, Grapperhaus CA, Bothe E, Bill E, Weyhermüller T, Neese F, Wieghardt K. J. Am. Chem. Soc. 2004; 126:5138–5153. [PubMed: 15099097]

61. Tomita T, Haruta N, Aki M, Kitagawa T, Ikeda-Saito M. J. Am. Chem. Soc. 2001; 123:2666–2667. [PubMed: 11456938]

62. Popescu V-C, Münck E, Fox BG, Sanakis Y, Cummings JG, Turner IM Jr, Nelson MJ. Biochemistry. 2001; 40:7984–7991. [PubMed: 11434767]

63. Hauser C, Glaser T, Bill E, Weyhermuller T, Wieghardt K. J. Am. Chem. Soc. 2000; 122:4352–4365.

64. Greene SN, Richards NGJ. Inorg. Chem. 2004; 43:7030–7041. [PubMed: 15500340]

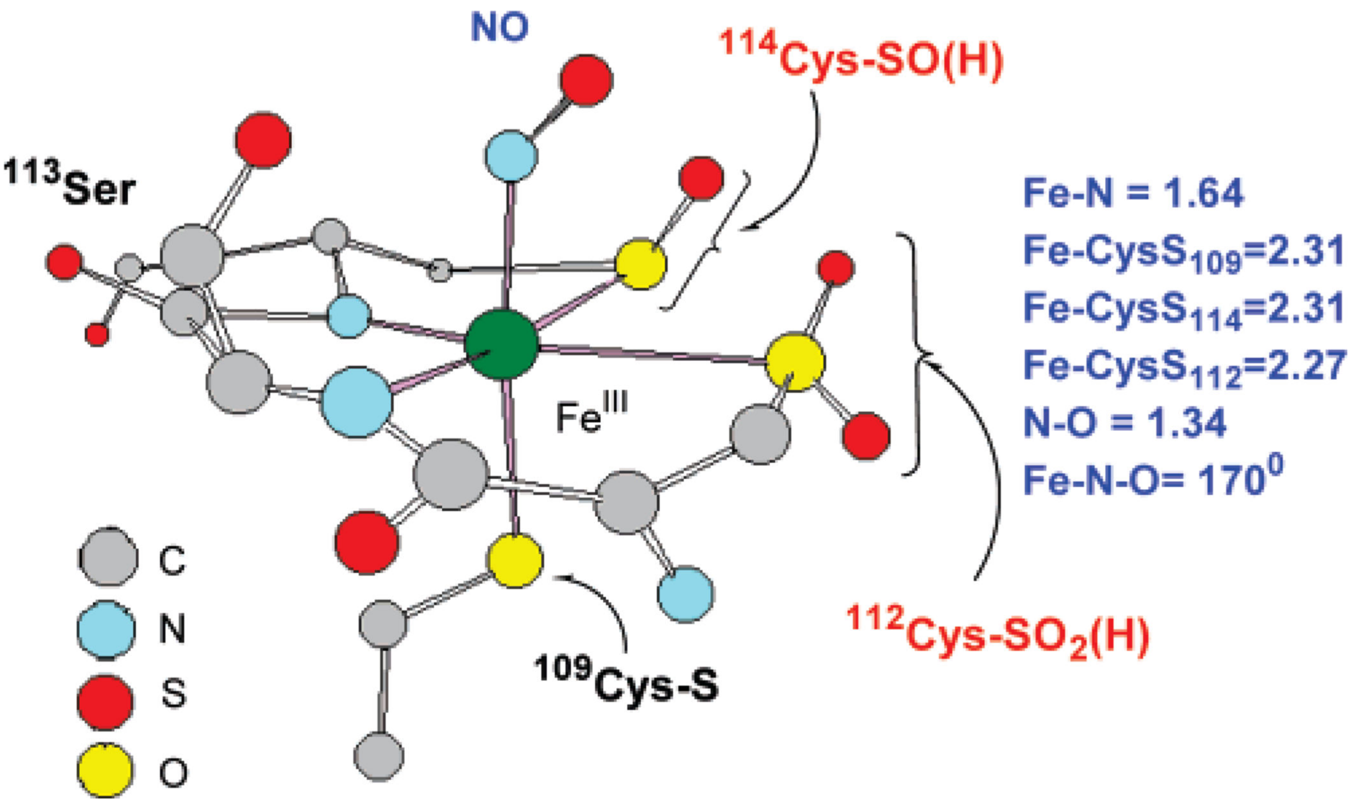

Figure 1.

Proposed active-site structure of NHase from the 1.7-Å resolution crystal structure.[3a]

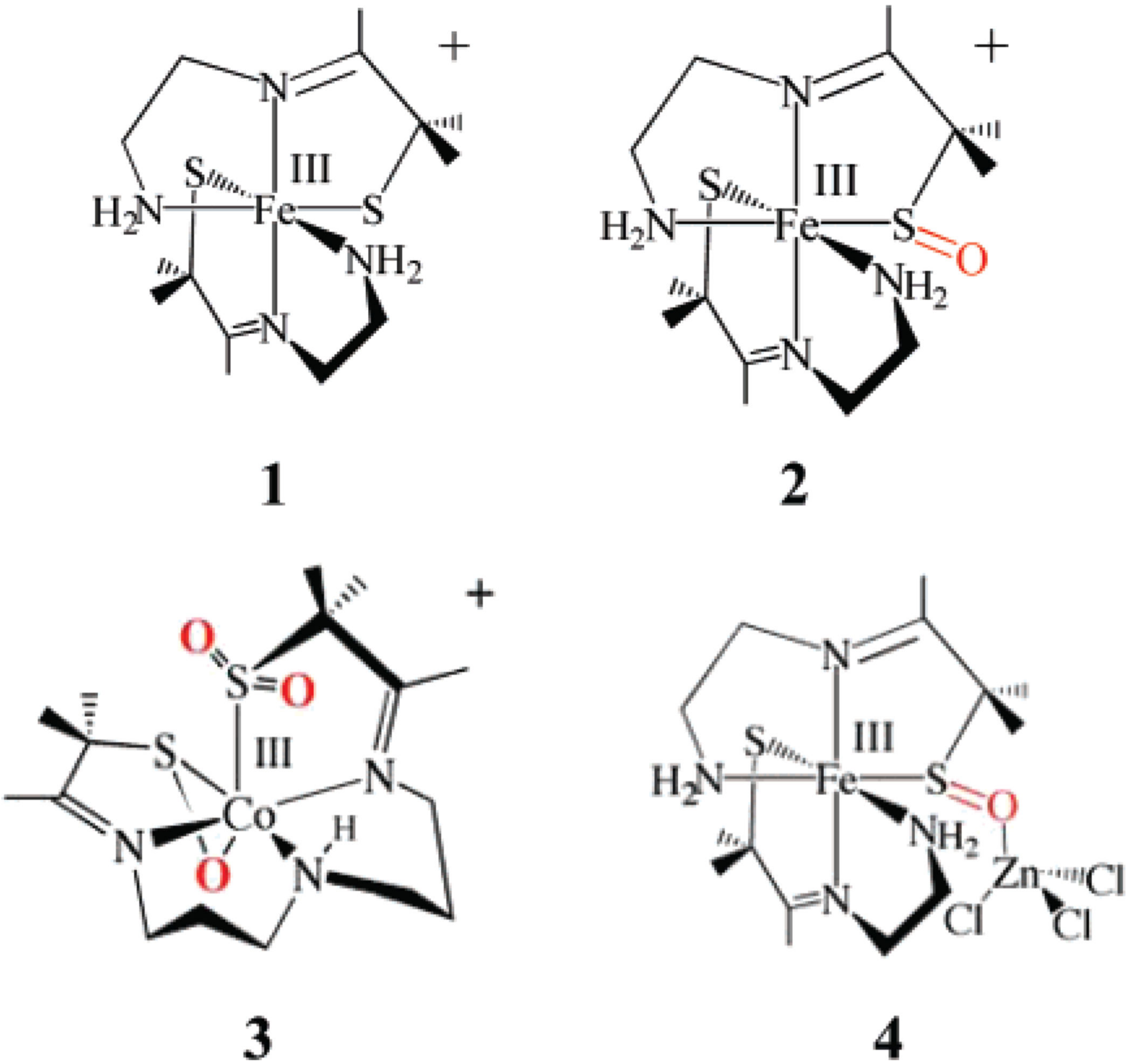

Figure 2.

Schematic structures of the model complexes of NHase studied.

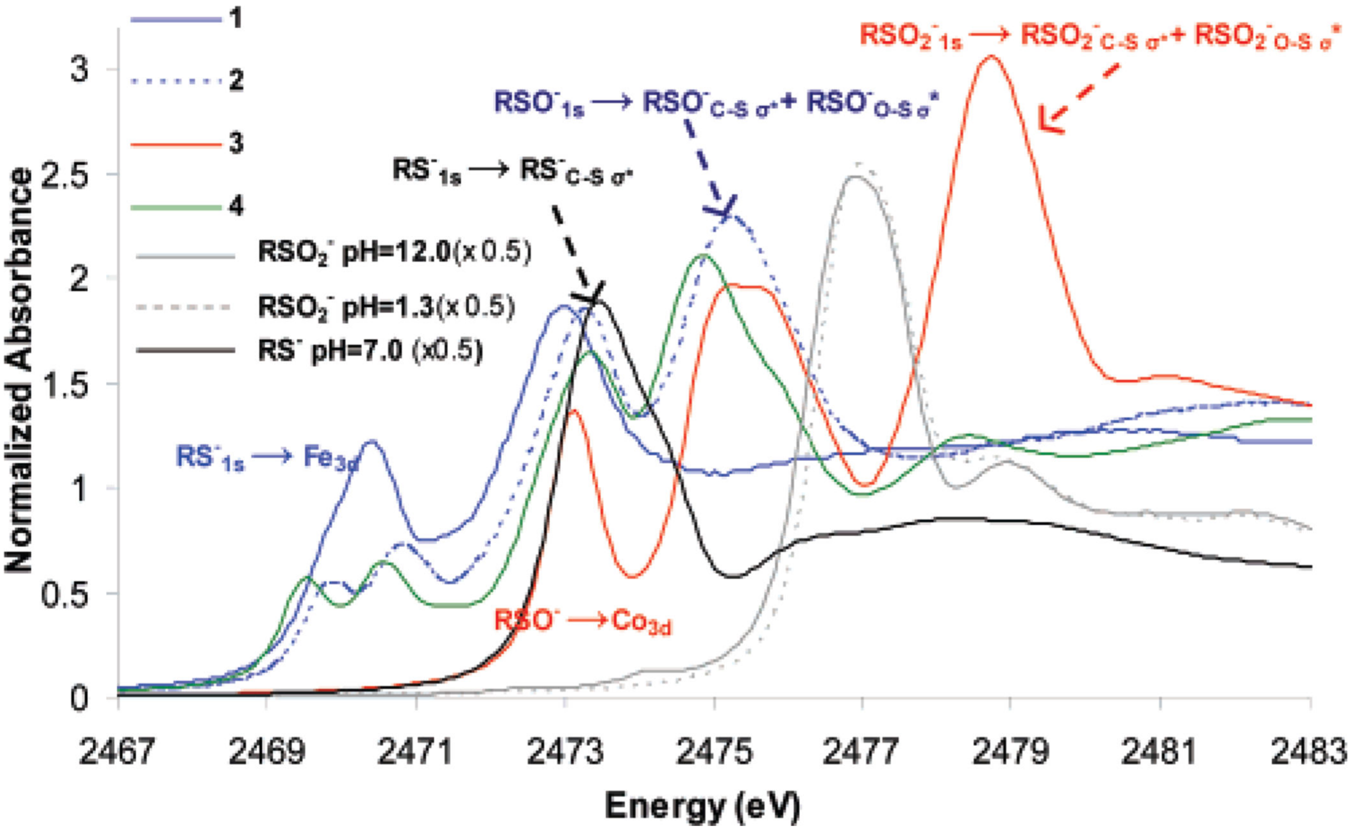

Figure 3.

S K-edge XAS of free cysteine at pH 7 (black), $OHCH_2SO_2^-$ (gray) and $OHCH_2SO_2H$ (dashed gray), and model complexes **1** (blue), **2** (dashed blue), **3** (red), and **4** (green).

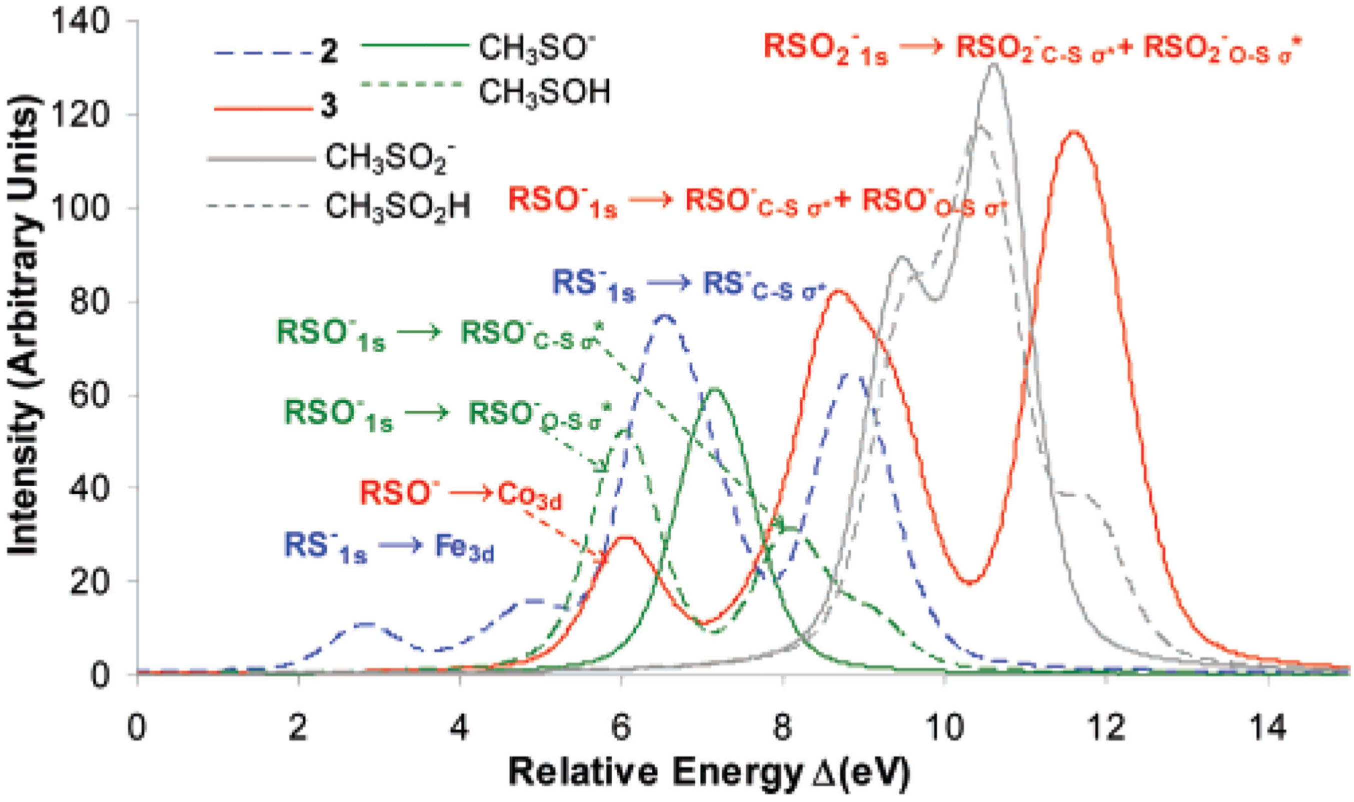

Figure 4.

DFT-calculated ground-state S_{3p} mixing in **2** (dashed blue), **3** (red), $CH_3SO_2^-$ (gray), CH_3SO_2H (dashed gray), CH_3SO^- (green), and CH_3-SOH (dashed green). Zero defined at 2390 eV.

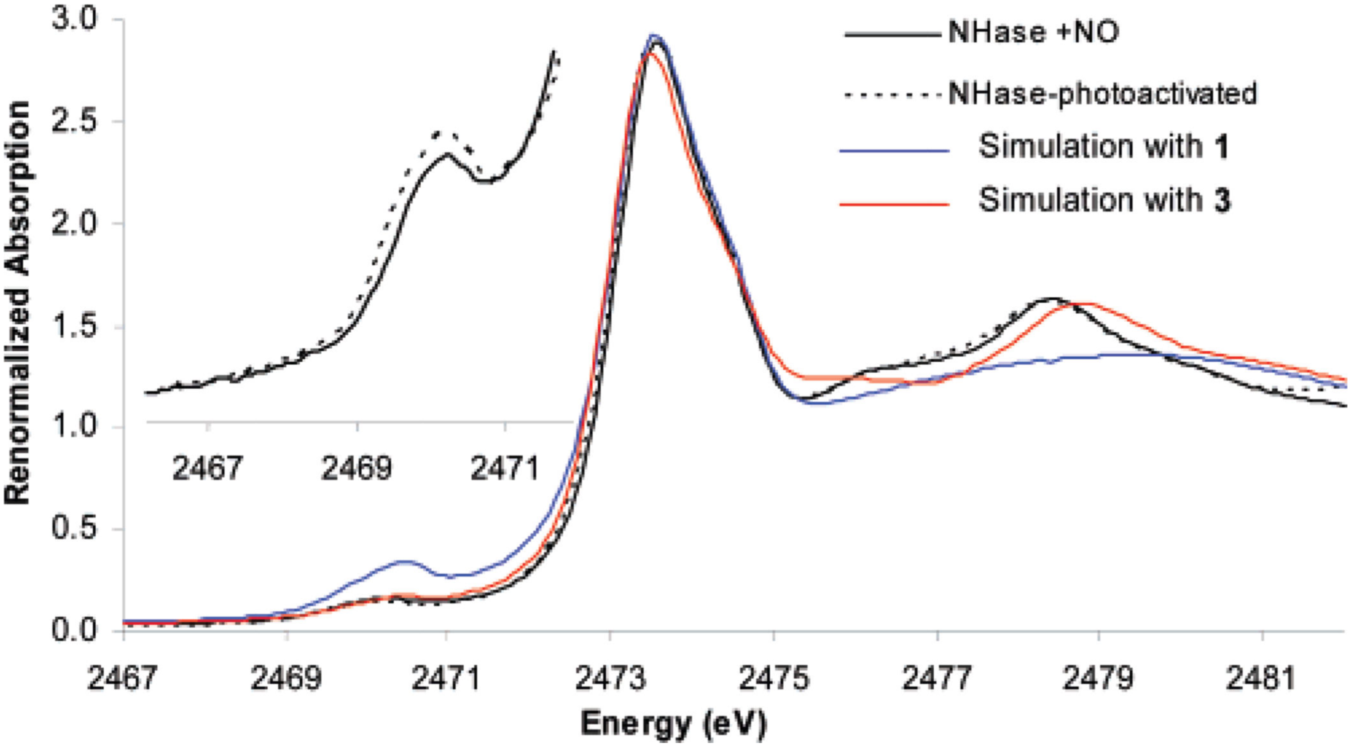

Figure 5.

S K-edge XAS of NHase-NO (black), NHase-photoactivated (dashed black), simulation with **1** only (blue), and simulation with **3** (red). Inset: Expanded pre-edge region of NHase-NO and NHase-photoactivated.

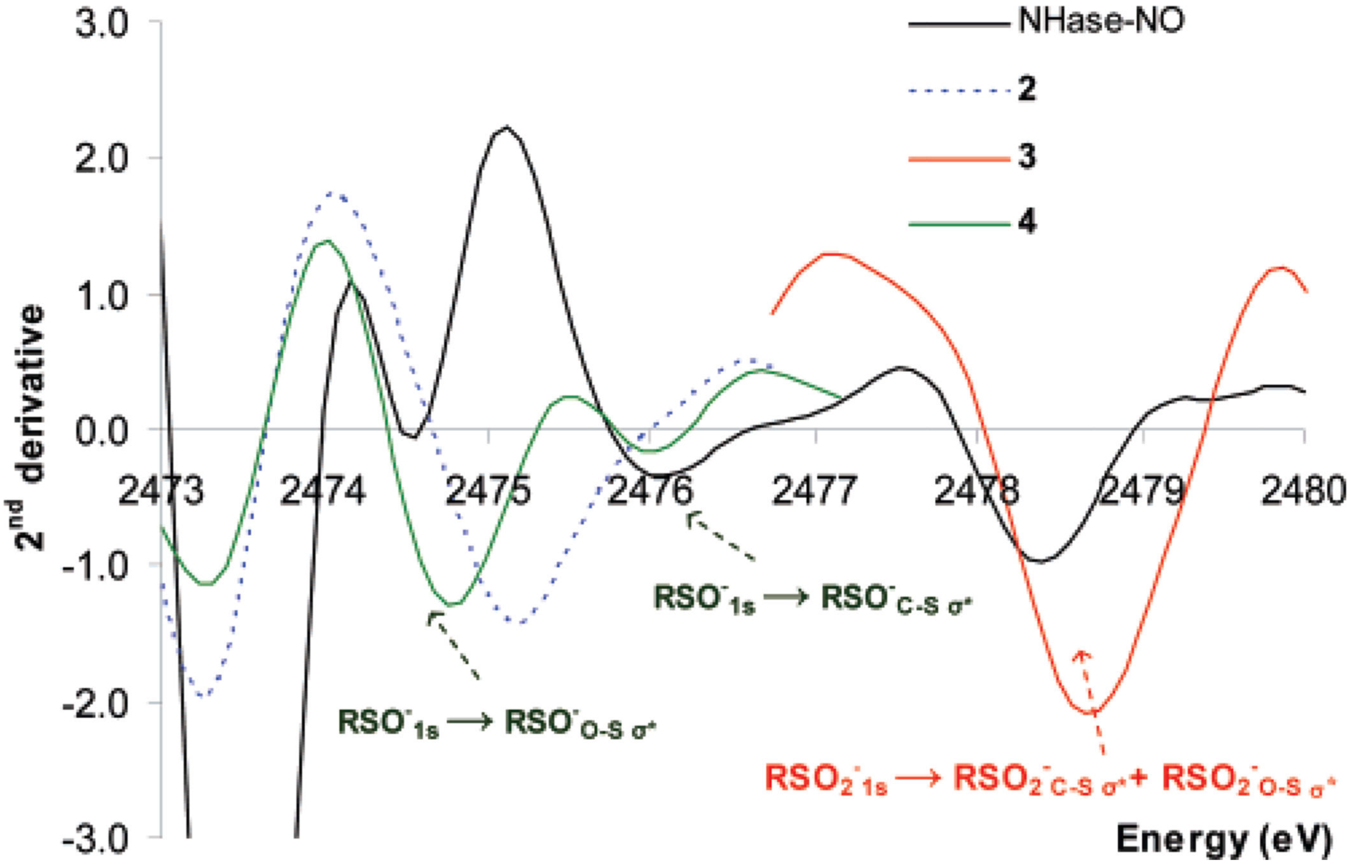

Figure 6.

Second derivative of XAS data of **2** (dashed blue), **3** (red), **4** (green), NHase-NO (black), and NHase-photoactivated (dashed black).

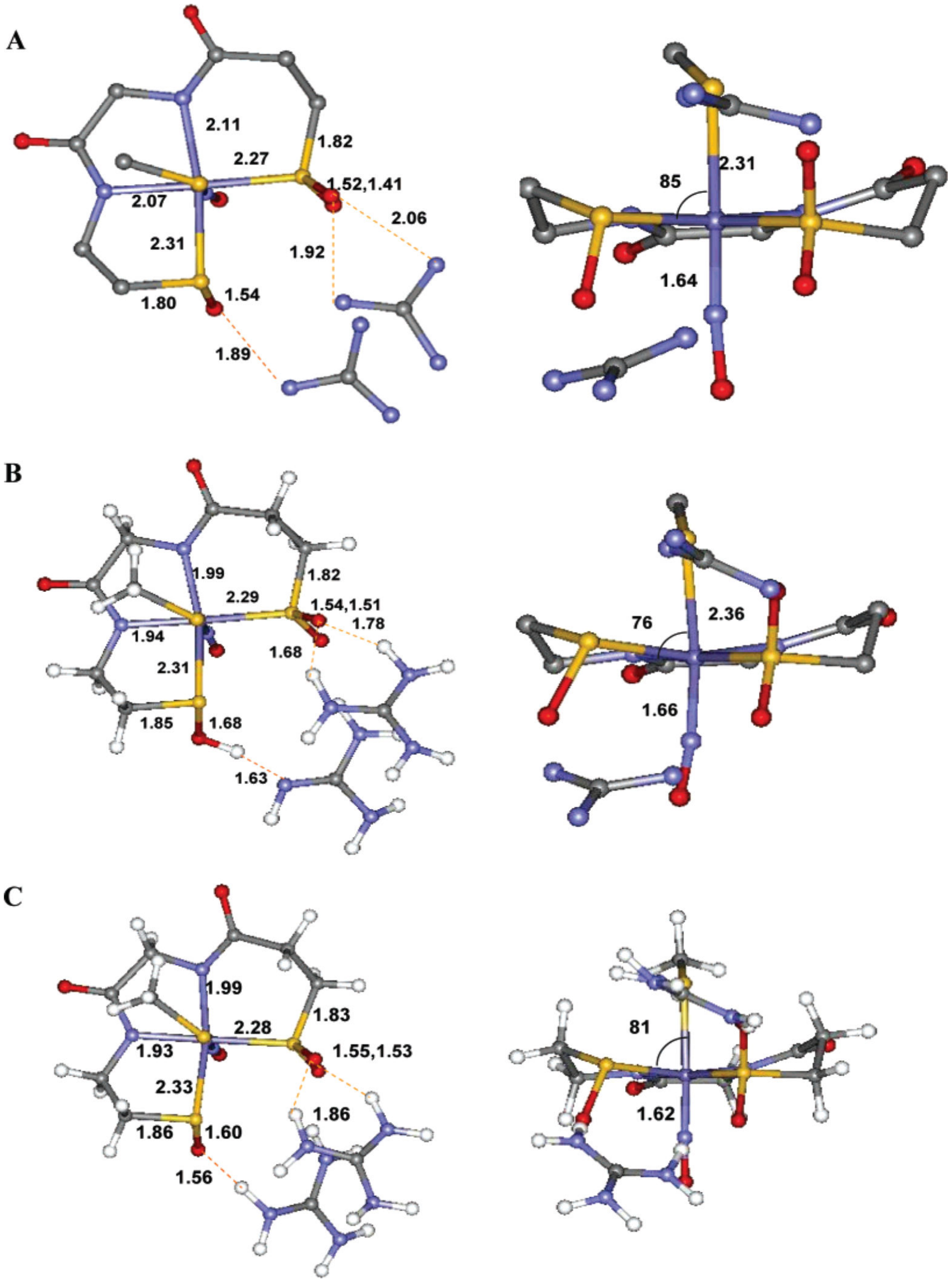

Figure 7.

(A) 1.6-Å resolution crystal structure of the NHase-NO complex active site. (B) Optimized geometry, gas phase. (C) Optimized geometry, PCM, ε = 4.0.

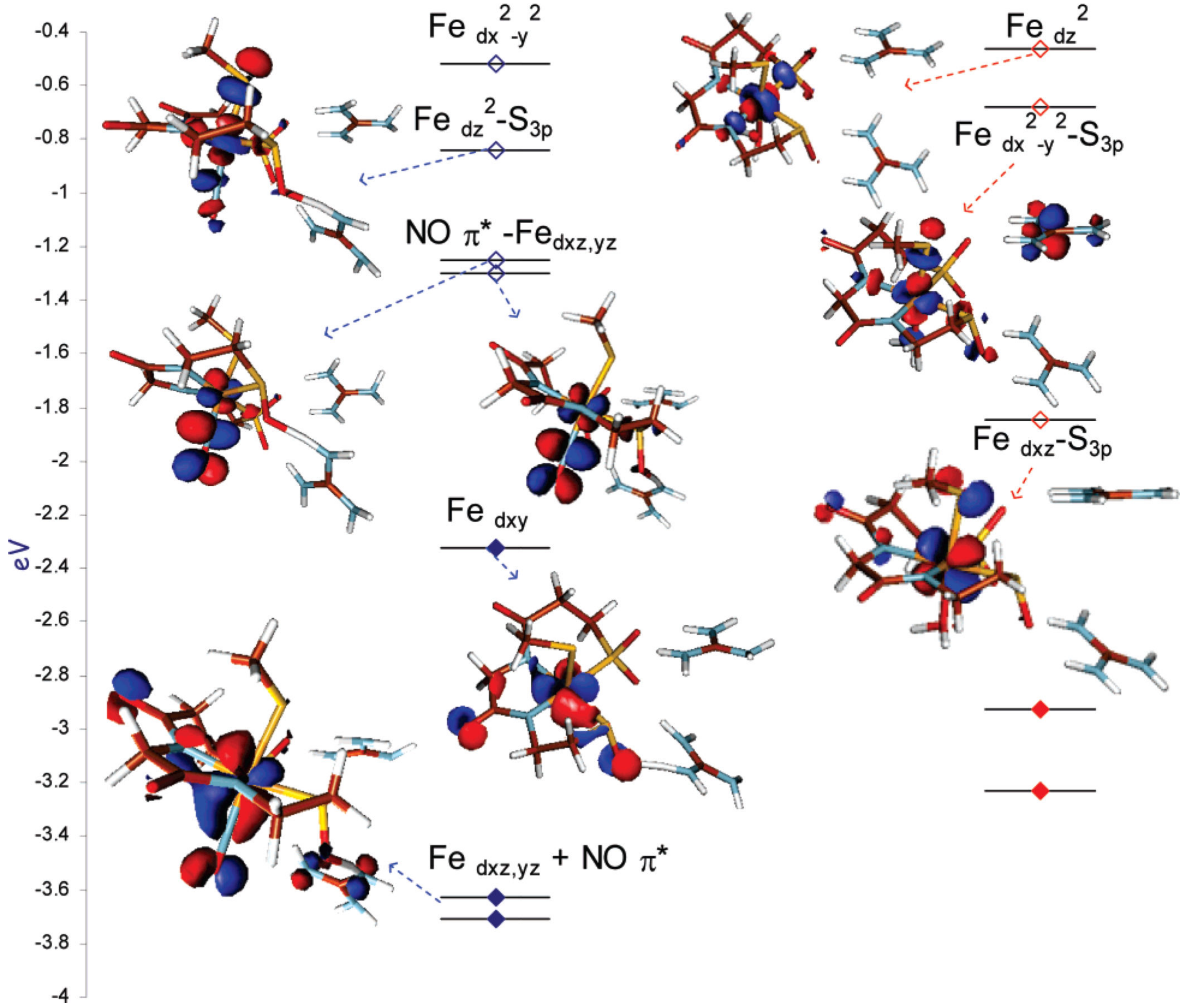

Figure 8.
DFT-calculated energy level diagram (β MO's) of the NHase-NO active site (left) and NHase-photoactivated (right) (occupied orbitals are filled diamonds and unoccupied orbitals are open diamonds). The MO's having S_{3p} mixing will have pre-edge transition intensity.

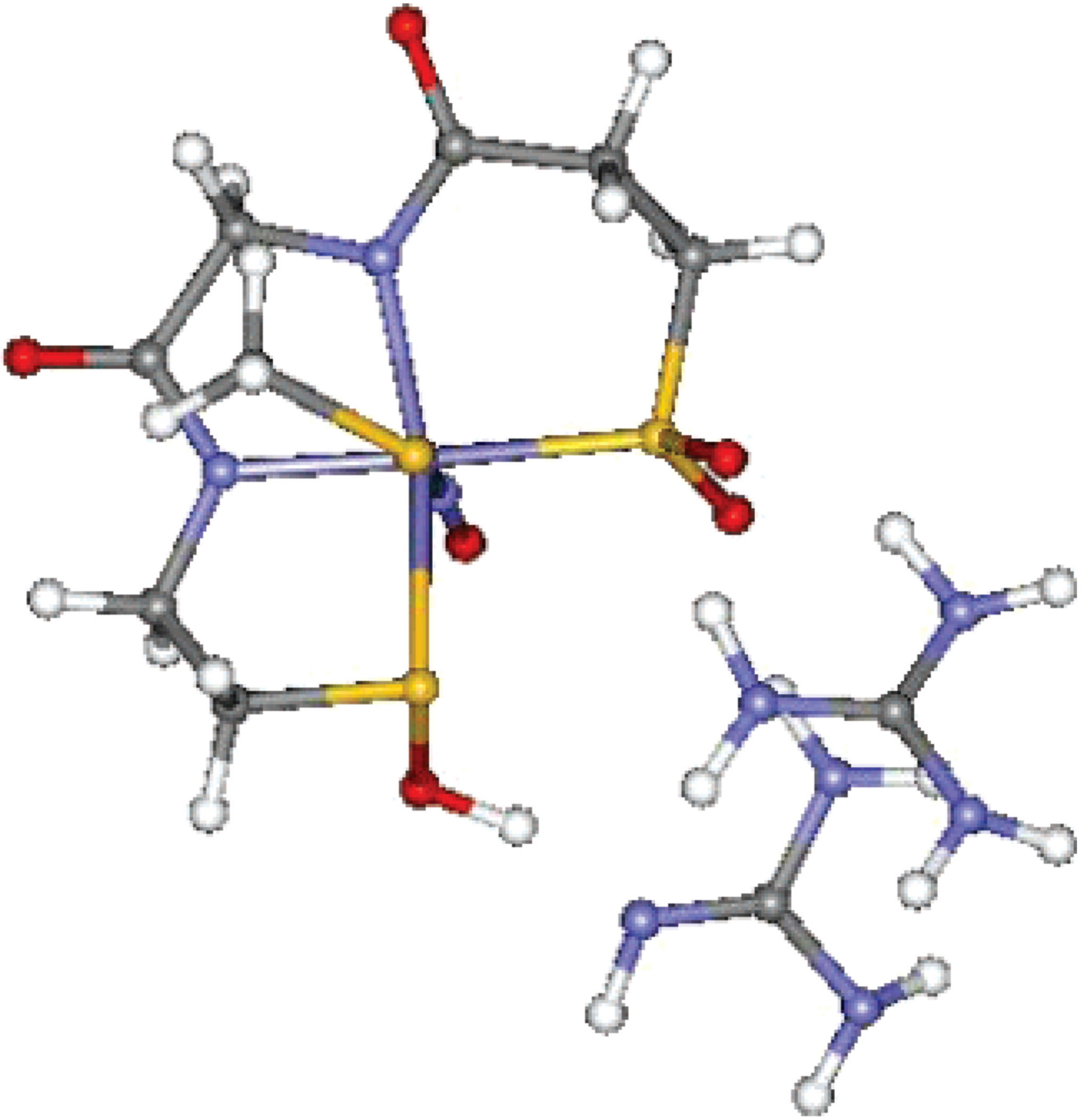

Figure 9.

Active-site model of NHase NO-bound form developed from S K-edge XAS and DFT calculations.

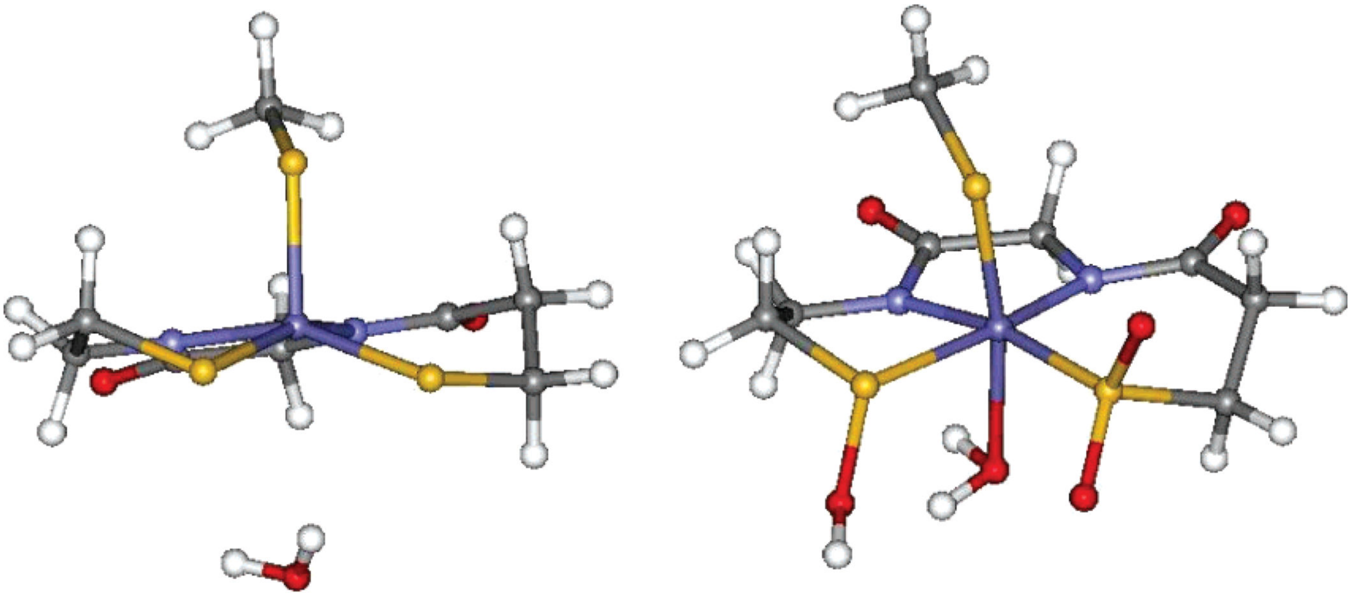

Figure 10.

(Left) H_2O binding at a hypothetical NHase site where cysteines are not oxidized; Fe–O = 3.4 Å. (Right) H_2O binding at the actual enzymatic site (Fe–O = 2.1 Å).

Table 1

DFT-Optimized Geometric Parameters[a]

	RS$^-$		RSO(H)			RSO$_2$(H)		
	M–S	**C–S**	**M–S**	**C–S**	**S–O**	**M–S**	**C–S**	**S–O**
Fe^{III}(ADIT)$_2$ (**1**)	2.21 (2.20)	1.84 (1.82)						
Fe^{III}(ADIT)(ADIT-O) (**2**)	2.19 (2.17)	1.85 (1.84)	2.31 (2.25)	1.87 (1.87)	1.55 (1.55)			
Co^{III}((η^2-SO)(SO$_2$)N$_3$ (Pr,Pr)) (**3**)			2.18 (2.13)	1.85 (1.83)	1.57 (1.55)	2.18 (2.12)	1.87 (1.86)	1.47 (1.46)
Fe^{III}(ADIT)(ADIT-O-ZnCl$_3$) (**4**)	2.20 (2.16)	1.84 (1.84)	2.29 (2.25)	1.86 (1.87)	1.56 (1.57)			
CH_3SO^-				1.86	1.60			
CH_3SOH				1.80	1.72			
CH_3SO^-- -$C(NH_2)_3^+$				1.82	1.64			
$CH_3SO_2^-$							1.90	1.53
CH_3SO_2H							1.81	1.49, 1.69

[a] Crystal structure parameters are given within parentheses.[19]

Table 2

Pre-edge Analysis Results for NHase Data

	Fe orbital			
	t_2		**e**	
	energy (eV)	**% S_{3p}**	**energy (eV)**	**% S_{3p}**
NHase-NO			2470.1	20
NHase-photoactivated	2469.6	9	2470.2	15